# Theoretical investigation of phonon polaritons in SiC micropillar resonators

Christopher R. Gubbin,[1] Stefan A. Maier,[2] and Simone De Liberato[1]
[1]*School of Physics and Astronomy, University of Southampton, Southampton, SO17 1BJ, United Kingdom*
[2]*Department of Physics, Blackett Laboratory, Imperial College London, London SW7 2AZ, United Kingdom*
(Received 20 October 2016; revised manuscript received 6 January 2017; published 30 January 2017)

Of late there has been a surge of interest in localized phonon polariton resonators which allow for the subdiffraction confinement of light in the midinfrared spectral region by coupling to optical phonons at the surface of polar dielectrics. Resonators are generally etched on deep substrates which support propagative surface phonon polariton resonances. Recent experimental work has shown that understanding the coupling between localized and propagative surface phonon polaritons in these systems is vital to correctly describing the system resonances. In this paper we comprehensively investigate resonators composed of arrays of cylindrical SiC resonators on SiC substrates. Our bottom-up approach, starting from the resonances of single, free-standing cylinders and isolated substrates, and exploiting both numerical and analytical techniques, allows us to develop a consistent understanding of the parameter space of those resonators, putting on firmer ground this blossoming technology.

DOI: 10.1103/PhysRevB.95.035313

## I. INTRODUCTION

Subdiffraction confinement of light is a necessity for miniaturization of optical devices and can be achieved by coupling photons to charged particles at interfaces over which the real part of the dielectric function changes sign. Predominantly free electrons, well described by a Drude-like dielectric function, are utilized [1]. As the Drude dielectric function is negative below the plasma frequency such materials provide broadband localization of light in modes termed surface plasmon polaritons, although this comes at the cost of high loss due to electron scattering. More recently subdiffraction confinement by coupling to crystal vibrations in the form of optical phonons in polar dielectrics has been demonstrated [2]. These materials have a negative dielectric function between the longitudinal and transverse optical phonon frequencies, in a region called the Reststrahlen band, and as the anharmonicity driven optical phonon damping occurs two orders of magnitude slower than electron damping in metals the resultant modes are comparatively long lived [3]. These modes are called surface phonon polaritons [4] and have morphology-dependent characteristics which allow for the tuning of modal frequencies and field profiles [5]. Their energies lie between the mid- and far-infrared, dependent on material choice, meaning these systems can make excellent narrow-band thermal sources [6,7]. Most recently, fabrication advancements have allowed the construction of user-defined cylindrical SiC nanoresonators on SiC substrates, which exhibit quality factors in excess of the theoretical limit for plasmonic resonators [8,9]. Only a few months ago the strong coupling between localized modes of user-defined cylindrical resonators and propagative surface phonon polaritons sustained by the substrate planar interface was demonstrated [10], highlighting how the resonant coupling between localized and propagative modes has to be taken into account to correctly describe the optical response of such systems. Surface phonon polaritons have also been utilized for a number of other applications like sensing [2], superlensing [11], near-field optics [12], and enhanced energy transfer between nanoparticles [13]. Surface phonon polaritons offer great promise as a test bed for integrated, midinfrared quantum photonics as a result of their long modal lifetimes and relative simplicity of fabrication.

To allow a fast development of this blossoming research field, in this paper we develop, using both analytical and numerical methods, a consistent understanding of the phonon polariton resonances of periodic arrays of cylindrical SiC resonators, of the kind that have been used in recent groundbreaking works [8–10]. The relative simple geometry of such samples allows us to methodically explore its parameter space, gaining both a quantitative understanding of those resonators, which can directly be experimentally exploited, and precious insight into the underlying physics, which can underpin investigations into to novel and more complex structures.

In a bottom-up approach we start our investigation in Sec. II by considering resonances of a free-standing cylindrical SiC resonator, analyzing how both the resonant frequencies and a number of figures of merit change with morphology. In Sec. III we consider the effect of a SiC substrate sitting below the cylinder, analyzing how the presence of phonon polaritons on the substrate surface modifies the resonant frequencies. Finally in Sec. IV we consider an array of cylindrical resonators over a substrate, where both the folding of surface modes due to the periodic patterning and the dipolar interaction between different pillars lead to the appearance of strongly dispersive features.

## II. FREE-STANDING CYLINDRICAL SiC RESONATOR

A single cylindrical resonator is characterized by two geometric parameters: its height $h$ and its diameter $d$. In the asymptotic limit $h \to \infty$ the system is exactly described by Mie-like theories and the resonator supports a predictable series of modes characterized by polarization and azimuthal phase dependency [14]. For finite $h$, Fabry-Pérot modes are supported along the length of the cylinder [15]. We are here interested in the modes of cylindrical SiC resonators with deeply subwavelength $h$ and $d$ which have recently been observed in reflectance measurements [8,10]. This system has no closed form analytical solution so we simulate numerically by finite element methods, using the RF module of COMSOL Multiphysics.

The SiC resonators are nonconservative systems with complex modal frequencies $\tilde{\omega}_m$ representing loss through energy

 

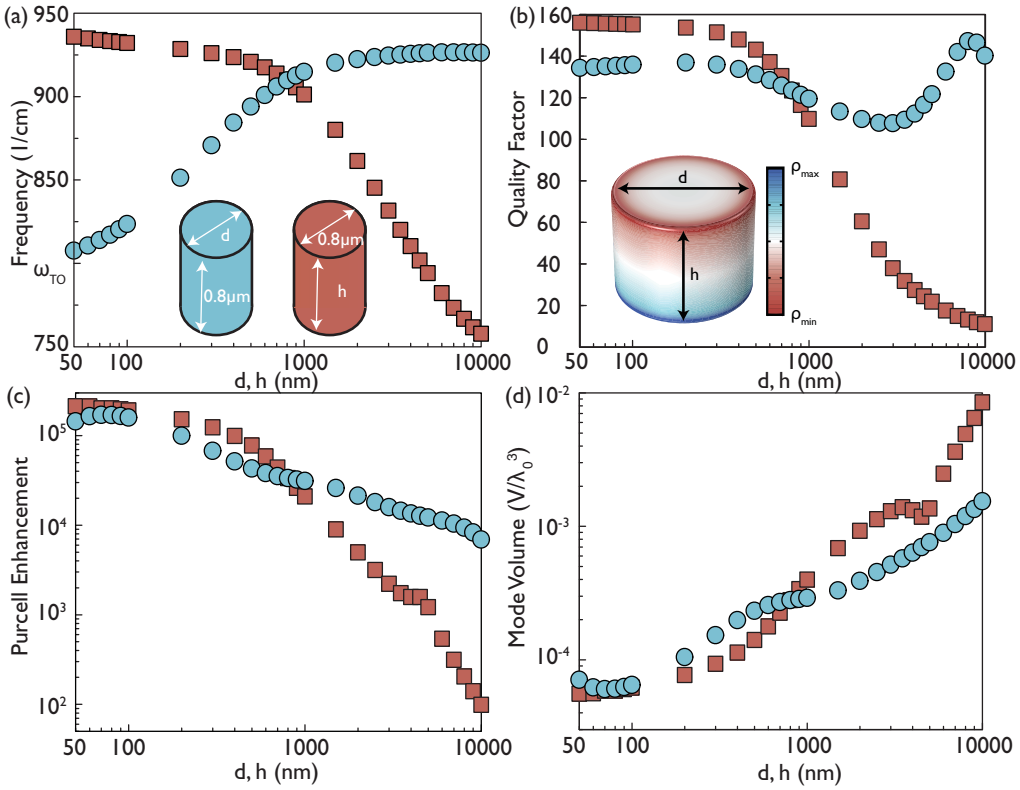


FIG. 1. (a) Real part of the resonant frequency of the longitudinal mode as a function of diameter at $h = 0.8$ $\mu$m height (circles) and as a function of height at $d = 0.8$ $\mu$m diameter (squares). (b) Quality factor of the longitudinal mode as a function of diameter at 0.8 $\mu$m height (circles) and as a function of height at 0.8 $\mu$m diameter (squares). Inset shows the surface charge distribution $\rho$ of the longitudinal mode for a cylinder of height $h = 0.8$ $\mu$m and diameter $d = 1$ $\mu$m. (c) Purcell enhancement of the longitudinal mode as a function of diameter at 0.8 $\mu$m height (circles) and as a function of height at 0.8 $\mu$m diameter (squares). (d) Mode volume of the longitudinal mode in units of the free space mode volume $\lambda_0^3$ as a function of diameter at 0.8 $\mu$m height (circles) and as a function of height at 0.8 $\mu$m diameter (squares).

leakage from the system. Even if intrinsic material losses are neglected, this leads to a non-Hermitian time-evolution operator for the isolated cylinder [16,17]. The modes of the system must thus be described in the formalism of quasinormal modes [18]. This is especially important when calculating the mode volume through the usual definition based on the systems electromagnetic energy

$$V = \frac{\int \epsilon(\mathbf{r})|\mathbf{E}(\mathbf{r})|^2 d^3\mathbf{r}}{2\epsilon_0 n^2 |\mathbf{E}(\mathbf{r}_{\max})|^2}, \tag{1}$$

where $\epsilon_0$ is the vacuum permittivity, $n$ the environment refractive index, $\epsilon(\mathbf{r})$ is the permittivity of the resonator and $\mathbf{E}(\mathbf{r})$ is the electric field of the mode with peak value $\mathbf{E}(\mathbf{r}_{\max})$. In systems possessing a complex modal frequency $\tilde{\omega}_m$ the fields diverge as $|\mathbf{r}| \to \infty$ resulting in divergence of the integral [19,20]. In addition the Kramers-Kronig consistency of the dielectric function means that loss necessarily results in a dispersive dielectric function, which leads to an alteration of the integral to account for energy in the matter [21]. These problems are solved by explicit calculation of the system quasinormal modes [18,22] which are normalized rigorously utilizing perfectly matched layers [23]. As described in Appendix A the quasinormal modes of the system are calculated utilizing the commercial finite element solver COMSOL Multiphysics to find the poles of the system response following the methods of Bai *et al.* [22].

For an electric field polarized parallel to the cylinder axis, the lowest lying mode has the surface charge distribution shown in the inset of Fig. 1(b). It corresponds to the fundamental Fabry-Pérot resonance of the $TM_0$ mode of the cylinder. This mode was first predicted for long silver nanowires by Takahara *et al.* [24] and corresponds in our case to the fundamental longitudinal dipolar resonance of the cylinder. This has been discussed extensively for SiC cylinders on substrates by Caldwell *et al.* where it is termed the monopolar mode [8,9]. We investigated the resonant frequency of this mode over the two-dimensional parameter space, with results shown in Fig. 1(a). The cylinder height is varied at a constant diameter $d = 0.8$ $\mu$m, and the diameter is varied at a constant height $h = 0.8$ $\mu$m, as schematically shown in the inset of Fig. 1(a). In the small diameter limit the resonant frequency tends to that of an infinite wire given by $\epsilon(\omega) \to -\infty$ at $\omega_{TO} = 797/\text{cm}$. As the cylinder diameter is increased the resonance tends toward an asymptote at $\approx 934/\text{cm}$, slightly blue shifted from the Fröhlich resonance at $\text{Re}[\epsilon(\omega)] = -2$. The quality factor over this range as shown in Fig. 1(b) is fairly flat because the length scale of the mode is unchanged. In the limit of vanishing height the longitudinal resonance should lie at the longitudinal optical (LO) phonon frequency $\omega_{LO} = 972/\text{cm}$ where $\epsilon(\omega) = 0$. Over the range shown in Fig. 1(a) a monotonous shift away from the LO phonon frequency is observed as expected for a Fabry-Pérot

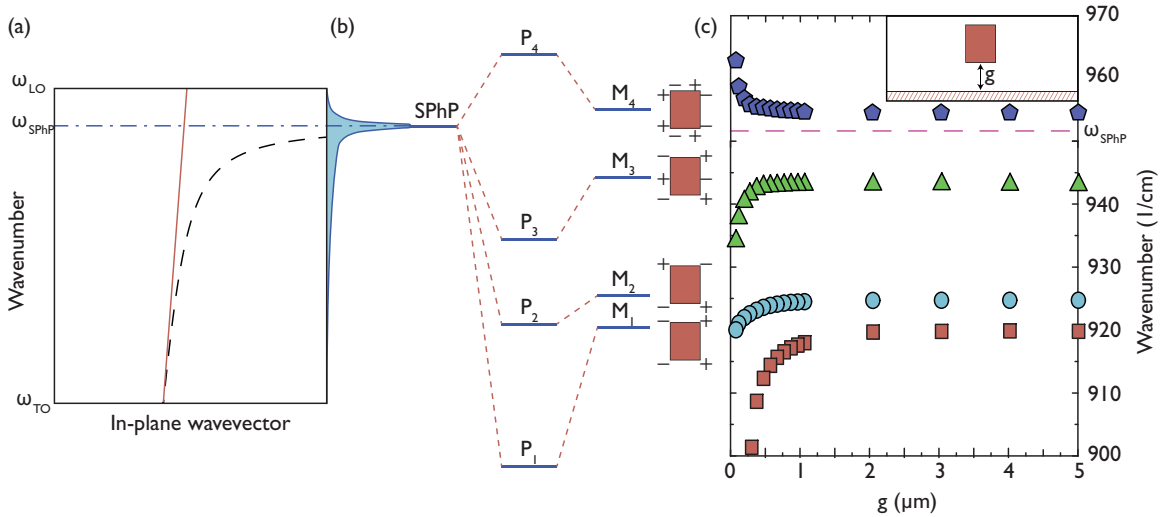


FIG. 2. (a) Dispersion of the surface phonon polariton mode supported by a vacuum/SiC interface is indicated by the black dashed line, the light cone by the red solid line, and the asymptotic surface phonon polariton frequency at $\omega_{\mathrm{SPhP}}$ by a blue dot-dashed line. The density of states is sketched on the right of the plot, peaking at $\omega_{\mathrm{SPhP}}$. (b) Shift caused by the coupling on the resonator modes. The uncoupled modes are the surface phonon polariton (SPhP) and the lowest lying four $m = 1$ modes of the resonator labeled $M_i, i = 1 - 4$. These interact to form coupled modes labeled $P_i$. The charge distributions of the four modes are indicated, the $M_1$ corresponds to the transverse dipole and $M_2$ to a transverse quadrupole resonance. (c) The transverse mode shifts as a cylindrical resonator of height 0.8 $\mu$m and diameter 1 $\mu$m is lowered onto a substrate.

resonance along the cylinder length being proportional to $1/h$. At around $h = 5$ $\mu$m the mode leaves the Reststrahlen band and the character of the resonance changes from a subdiffraction localized phonon polariton to a that of a high-index dielectric resonator. This transition is accompanied by the drop in the quality factor observed in Fig. 1(b). The Purcell enhancement is evaluated for an emitter 5 nm from the cylinder edge; the results are shown in Fig. 1(c), and the procedure used to calculate it, taking care of the effect of losses, is outlined in Appendix A. Mode volumes are given in Fig. 1(d). Smaller resonators allow a tighter confinement of the field and correspondingly larger Purcell enhancements, exceeding $10^5$ in the small resonator limit. The dip in the height scanned data at $h = 4$ $\mu$m occurs as the mode energy crosses the transverse optic (TO) phonon energy, being evanescent in nature for smaller heights and diffraction limited for larger.

This section has focused on the longitudinal mode which is azimuthally invariant, meaning its azimuthal mode number $m = 0$. Modes with higher azimuthal mode numbers are supported with angular dependance $e^{im\phi}$ where $\phi$ is the azimuthal angle. In Appendix B we include a similar study for the lowest lying $m = 1$ mode which will be referred to as the transverse dipolar mode in accordance with Caldwell *et al.* [8] and consists of parallel dipoles excited at each cylinder end facet. In this case Purcell enhancements exceeding $10^6$ are achievable due to tighter confinement of the mode at the cylinder vertices. For each azimuthal number $m$ higher order modes are also supported with differing phase changes along the long axis.

## III. CYLINDRICAL SiC RESONATOR ON A SiC SUBSTRATE

In the previous section we considered the resonances of a single SiC cylinder in vacuum. The following step toward a consistent description of real resonators is to consider the effect of placing the cylinders on a SiC substrate. A planar, optically thick SiC substrate in vacuum supports a propagating surface phonon polariton (SPhP) with dispersion

$$\mathbf{k}_{\parallel} = \frac{\omega}{c}\sqrt{\frac{\epsilon(\omega)}{\epsilon(\omega)+1}}, \tag{2}$$

where $\mathbf{k}_{\parallel}$ is the in-plane wave vector, $\epsilon(\omega)$ is the dispersive dielectric function of the substrate, and $c$ is the speed of light. The dispersion is plotted in Fig. 2(a), where it is clearly visible that in the nonretarded regime the majority of the oscillator strength lies at the asymptotic frequency $\omega_{\mathrm{SPhP}} = \omega_{\mathrm{TO}}\sqrt{\frac{1+\epsilon_0}{1+\epsilon_\infty}} \approx 951/\mathrm{cm}$. For definiteness in the remainder of this section we consider cylinders of diameter $d = 1$ $\mu$m and height $h = 0.8$ $\mu$m. For these parameters the bright transverse and longitudinal resonances lie at lower energies than the asymptote of the surface mode $\omega_{\mathrm{SPhP}}$.

While the cylinder-substrate separation is large enough, cylinder and substrate modes are good approximations for the modes of the coupled system. This ceases to be true for submicron distances, when the overlap of the resonator and surface modes cannot be neglected. Their resulting coupling leads to repulsion between the different modes, which shift as illustrated schematically in Fig. 2(b). To illustrate this process we carry out finite element simulations of the first four $m = 1$ modes of SiC cylinders discussed in Sec. I, separated from a substrate by a gap of width $g$. The relevant surface charge distribution for the different uncoupled modes of the cylinder are sketched on the left of Fig. 2(c), where $M_1$ is the transverse dipolar mode, and $M_2$, $M_3$, and $M_4$ are the following higher lying $m = 1$ modes. We plot the real parts of the resonant frequency in Fig. 2(c). As the resonator-substrate separation $g$ vanishes, all the modes lying below the asymptotic frequency

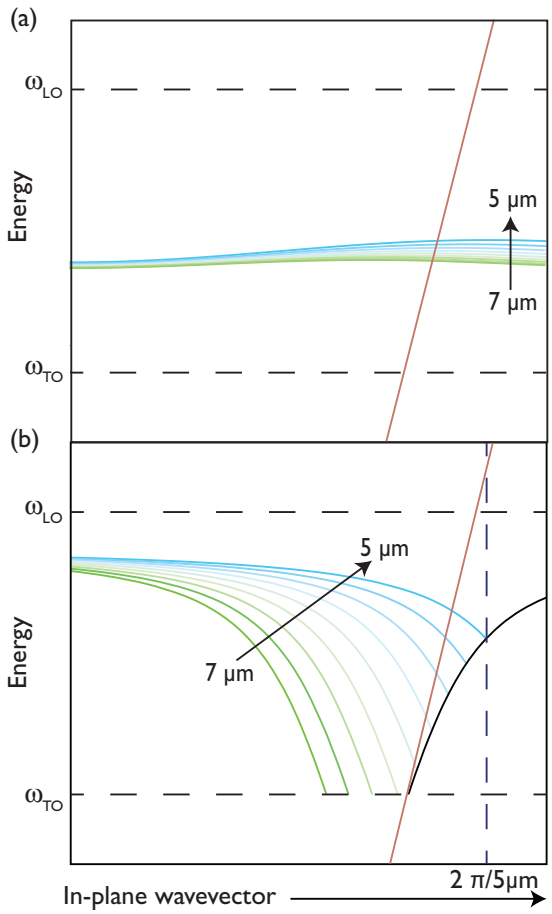


FIG. 3. (a) Tight binding dispersion of the monopolar mode for a range of array periods from 5 to 7 $\mu$m. (b) Dispersion of the first folded surface phonon polariton branch at a SiC/vacuum interface, illustrated by the colored lines for array pitches between 5 and 7 $\mu$m. The edge of the first Brillouin zone is illustrated by the dashed vertical line for period 5 $\mu$m, while the horizontal dashed lines show the borders of the Reststrahlen band.

$\omega_{\mathrm{SPhP}}$ are observed to red shift while those above blue shift. This is as expected for modes which interact with a delocalized surface mode at $\omega_{\mathrm{SPhP}}$ [25].

## IV. ARRAY OF CYLINDRICAL SiC RESONATORS ON A SiC SUBSTRATE

When the substrate is periodically patterned, a more in-depth analysis is needed as the normal modes of the system will now be given by Bloch waves delocalized over the array. On one hand this can lead to dispersive features in the dispersion of the localized phonon polaritons, due to dipolar coupling between the different cylinders. Such an effect can be captured by a tight binding model, which we already described in Ref. [10]. This procedure, whose details can be found in Appendix C, lead to frequencies for the monopolar and transverse dipolar modes dependent upon the in-plane wave vector. While this effect is important for the monopolar mode, as shown in Fig. 3(a), it is negligible for the transverse modes. This can be understood noticing that, as shown in Ref. [8], the charge imbalance of the transverse modes is localized in the cylinders whereas the monopolar mode induces a charge imbalance between the cylinders and the substrate, thus efficiently coupling the cylinders between them. In the following we will assume that all transverse modes are dispersionless for the array periods considered.

On the other hand the periodicity of the array causes the dispersion of the surface modes bound to the substrate to be folded back into the first Brillouin zone of the lattice, thus existing at experimentally accessible wave vectors within the light cone. This folding as a function of array periodicity is illustrated in Fig. 3(b) for square arrays of varying period. Such a tunability can bring the localized and surface modes in resonance, and their coupling cannot be reduced to a simple shift as in the previous section, but it becomes necessary to consider the hybridization of the different bare modes. To do this we use an extension of the Hopfield theory we used in Ref. [10]. Notice that while we recently also developed an extension of the Hopfield theory to inhomogeneous, lossy media [26], capable of giving a description of the resonances without adjustable parameters, and including losses in a more consistent and fundamental way, here we prefer to rely on numerical simulations to fit the coupling parameters and to use real frequencies instead of complex ones, calculating linewidths only in a second step, as this method is more transparent and readily applicable to the design and optimization of resonator samples. Our approximate results will then be compared with numerical simulations performed using the quasinormal mode theory described in Appendix A.

When only a single branch of the folded SPhP lies in the neighborhood of the resonator lower laying modes, the system, neglecting losses, may be described by a Hamiltonian composed of two terms. The first

$$\mathcal{H}_0 = \hbar \sum_{\mathbf{k}_\parallel} [\omega^m_{\mathbf{k}_\parallel} \hat{a}^\dagger_{\mathbf{k}_\parallel} \hat{a}_{\mathbf{k}_\parallel} + \omega^{t1} \hat{b}^\dagger_{\mathbf{k}_\parallel} \hat{b}_{\mathbf{k}_\parallel} + \omega^{t2} \hat{c}^\dagger_{\mathbf{k}_\parallel} \hat{c}_{\mathbf{k}_\parallel} + \omega^s_{\mathbf{k}_\parallel} \hat{d}^\dagger_{\mathbf{k}_\parallel} \hat{d}_{\mathbf{k}_\parallel}], \tag{3}$$

describes the uncoupled modes, where $\mathbf{k}_\parallel$ is the in-plane wave vector, $\omega^m_{\mathbf{k}_\parallel}$ is the real part of the dispersive frequency of the monopolar mode obtained by the tight-binding approach described in Appendix C, $\omega^{t1}$ and $\omega^{t2}$ the real parts of the frequencies of the two lowest transverse $m = 1$ modes, $\omega^s_{\mathbf{k}_\parallel}$ the real part of the surface mode from Eq. (2), and $\hat{a}_{\mathbf{k}_\parallel}$, $\hat{b}_{\mathbf{k}_\parallel}$, $\hat{c}_{\mathbf{k}_\parallel}$, $\hat{d}_{\mathbf{k}_\parallel}$ are the respective annihilation operators obeying bosonic commutation rules. The second term describes instead the coupling between surface and resonator modes

$$\mathcal{H}_{\mathrm{int}} = \hbar \sum_{\mathbf{k}_\parallel} [f_0(\hat{a}^\dagger_{\mathbf{k}_\parallel} \hat{d}_{\mathbf{k}_\parallel} + \hat{d}^\dagger_{\mathbf{k}_\parallel} \hat{a}_{\mathbf{k}_\parallel}) + g_0(\hat{b}^\dagger_{\mathbf{k}_\parallel} \hat{d}_{\mathbf{k}_\parallel} + \hat{d}^\dagger_{\mathbf{k}_\parallel} \hat{b}_{\mathbf{k}_\parallel}) + h_0(\hat{c}^\dagger_{\mathbf{k}_\parallel} \hat{d}_{\mathbf{k}_\parallel} + \hat{d}^\dagger_{\mathbf{k}_\parallel} \hat{c}_{\mathbf{k}_\parallel})], \tag{4}$$

where $f_0$, $g_0$, and $h_0$ are the coupling rates of the monopole and lowest two transverse modes, respectively, with the quasiresonant surface branch. The rotating-wave approximation has been used, as the condition $f_0, g_0, h_0 \ll \omega^m_{\mathbf{k}_\parallel}, \omega^{t1}, \omega^{t2}, \omega^s_{\mathbf{k}_\parallel}$ is safely satisfied, with a coupling to frequency ratio of

the order of $10^{-2}$ [10]. The normal modes of the coupled system $\mathcal{H} = \mathcal{H}_0 + \mathcal{H}_{\text{int}}$ can be expressed in the form of linear superpositions of the bare modes

$$\hat{Y}^i_{\mathbf{k}_\parallel} = m^i_{\mathbf{k}_\parallel}\hat{a}_{\mathbf{k}_\parallel} + n^i_{\mathbf{k}_\parallel}\hat{b}_{\mathbf{k}_\parallel} + o^i_{\mathbf{k}_\parallel}\hat{c}_{\mathbf{k}_\parallel} + p^i_{\mathbf{k}_\parallel}\hat{d}_{\mathbf{k}_\parallel}, \tag{5}$$

where the Hopfield coefficients $m^i_{\mathbf{k}_\parallel}$, $n^i_{\mathbf{k}_\parallel}$, $o^i_{\mathbf{k}_\parallel}$ $p^i_{\mathbf{k}_\parallel}$ can be found solving the eigenproblem

$$\left[\mathcal{M}_{\mathrm{k}_\parallel} - \omega^{\mathrm{i}}_{\mathbf{k}_\parallel}\right]\begin{pmatrix} m^i_{\mathbf{k}_\parallel} \\ n^i_{\mathbf{k}_\parallel} \\ o^i_{\mathbf{k}_\parallel} \\ p^i_{\mathbf{k}_\parallel} \end{pmatrix} = 0, \tag{6}$$

where $\mathcal{M}_{k_\parallel}$ is the Hopfield matrix

$$\mathcal{M}_{k_\parallel} = \begin{pmatrix} \omega^m_{\mathbf{k}_\parallel} & 0 & 0 & f_0 \\ 0 & \omega^{t1} & 0 & g_0 \\ 0 & 0 & \omega^{t2} & h_0 \\ f_0 & g_0 & h_0 & \omega^s_{\mathbf{k}_\parallel} \end{pmatrix}, \tag{7}$$

and the eigenvalue $\omega^i_{\mathbf{k}_\parallel}$ is here to be interpreted as the real part of the $i$th quasinormal mode frequency $\tilde{\omega}^i_{\mathbf{k}_\parallel}$. Results for array periods 6, 6.5, and 7 $\mu$m, are shown in Figs. 4(a)–4(c), where the symbols represent the real part of the complex quasimode frequencies obtained through the numerical procedure described in Appendix A, and the solid lines are obtained by solving Eq. (6) and fitting for $\omega^{t1}$,$\omega^{t2}$, $f_0$, $g_0$, $h_0$, and the $\alpha$ and $\zeta$ parameters described in Appendix C. The plots are truncated before the edge of the first Brillouin zone to avoid inclusion of additional SPhP branches.

Excellent agreement is achieved between the two approaches. The peak Rabi frequency calculated is 15.84/cm, representing ≈2% of the bare mode energy. The calculated frequencies for the highest energy polariton branch are systematically lower in the fitted data; this is due to coupling of the surface mode to higher energy, closely spaced resonances near the asymptotic SPhP frequency which have been omitted for simplicity from the Hopfield diagonalization. The Hopfield coefficients weighting the bare components of the four coupled modes are shown in Figs. 5(a)–5(d) for an array period of 6 $\mu$m, from which it is clear that a substantial hybridization between the different modes occurs.

As the polaritonic modes are linear superpositions of the bare modes, their linewidths are expected to vary predictably as sums of the linewidths of the bare modes weighted by the square of the Hopfield coefficients [27]. The linewidth of the $i$th coupled mode can thus be written in terms of the linewidths of the bare modes $\Gamma^m_{\mathbf{k}_\parallel}$,$\Gamma^{t1}_{\mathbf{k}_\parallel}$,$\Gamma^{t2}_{\mathbf{k}_\parallel}$, and $\Gamma^s_{\mathbf{k}_\parallel}$ and of the Hopfield coefficients as

$$\Gamma^i_{\mathbf{k}_\parallel} = |m^i_{\mathbf{k}_\parallel}|^2\Gamma^m_{\mathbf{k}_\parallel} + |n^i_{\mathbf{k}_\parallel}|^2\Gamma^{t1}_{\mathbf{k}_\parallel} + |o^i_{\mathbf{k}_\parallel}|^2\Gamma^{t2}_{\mathbf{k}_\parallel} + |p^i_{\mathbf{k}_\parallel}|^2\Gamma^s_{\mathbf{k}_\parallel}, \tag{8}$$

which can be fitted to the imaginary part of the modal frequency calculated using the approach detailed in Appendix A. Numerical results for array periods 6, 6.5, and 7 $\mu$m are given by the symbols in Fig. 6. The dispersive surface mode linewidth is taken from Eq. (2) and the known dielectric function. Fits are carried out for the two transverse linewidths $\Gamma^{t1}_{\mathbf{k}_\parallel}$,$\Gamma^{t2}_{\mathbf{k}_\parallel}$ and for the monopolar linewidth. The monopole linewidth is dispersive and fits to a phenomenological $a + b\mathbf{k}\|^2$ relationship, verified by fitting to the dispersive monopole linewidth in the absence of the substrate. The results are given by the solid lines in Fig. 6.

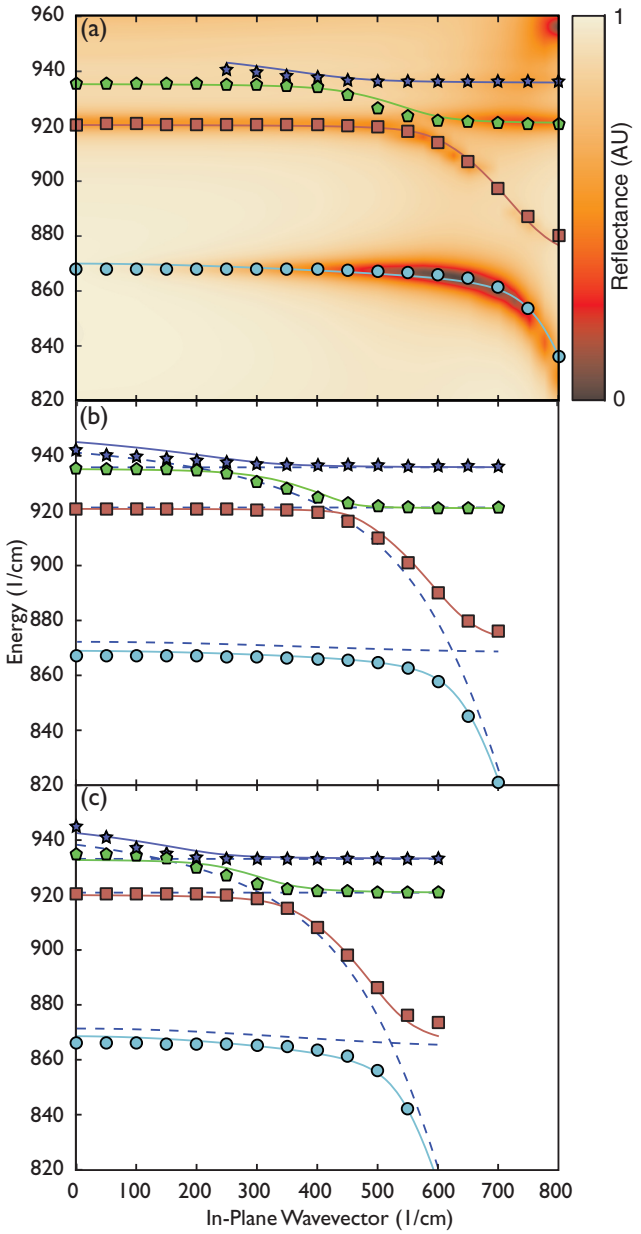


FIG. 4. Resonances of the pillar array coupled to the substrate as a function of the in-plane wave vector for array periods (a) 6 $\mu$m, (b) 6.5 $\mu$m, and (c) 7 $\mu$m. The symbols represent the real parts of the frequencies of the four coupled eigenmodes calculated using quasimode theory as from Appendix A. The solid lines are instead the fits obtained solving Eq. (6). Each plot is truncated to restrict to the first Brillouin zone. Dotted lines represent the dispersions of the bare mode. Panel (a) is overlaid on a reflectance map calculated by finite element simulations to demonstrate the accuracy of the numerical methods employed.

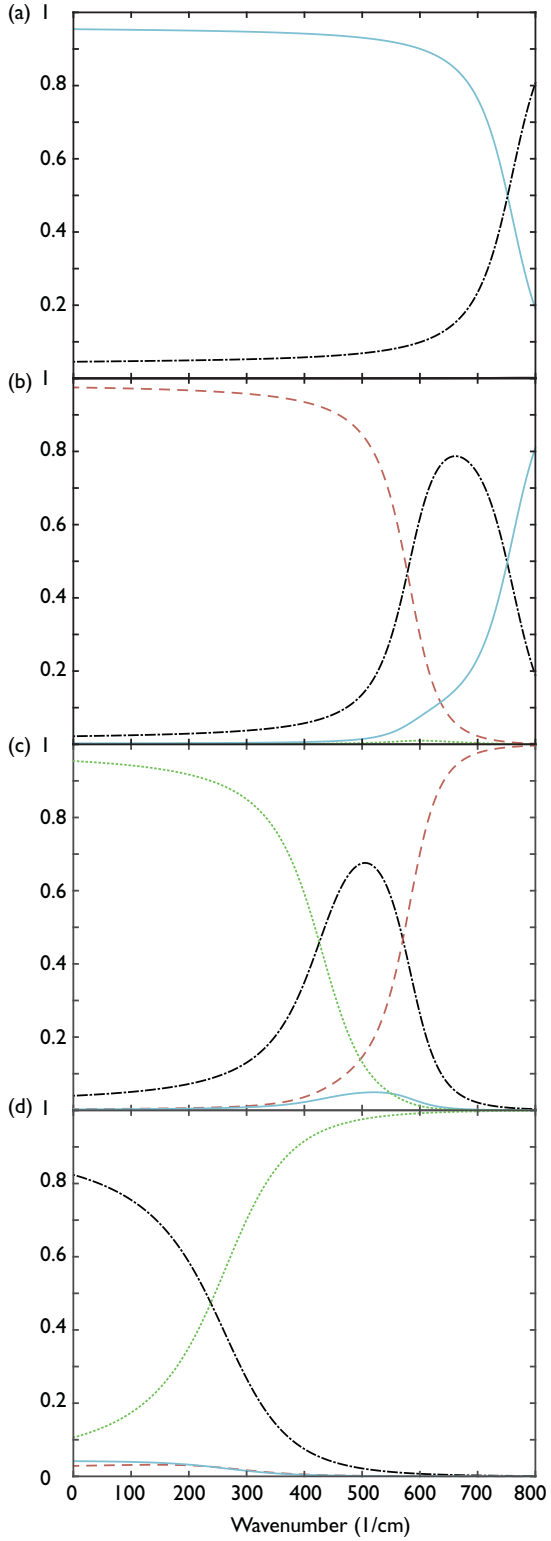


FIG. 5. Absolute magnitude of the Hopfield coefficients for array period 6 $\mu$m. Panels (a)–(d) show the bare components of each coupled mode individually, in order of ascending energy. The solid line represents the monopole coefficient, dashed the dipole transverse, dotted the quadrupole transverse, and dot-dashed the surface mode.

Surprisingly good agreement between theory and numerics is achieved despite the simplicity of the model.

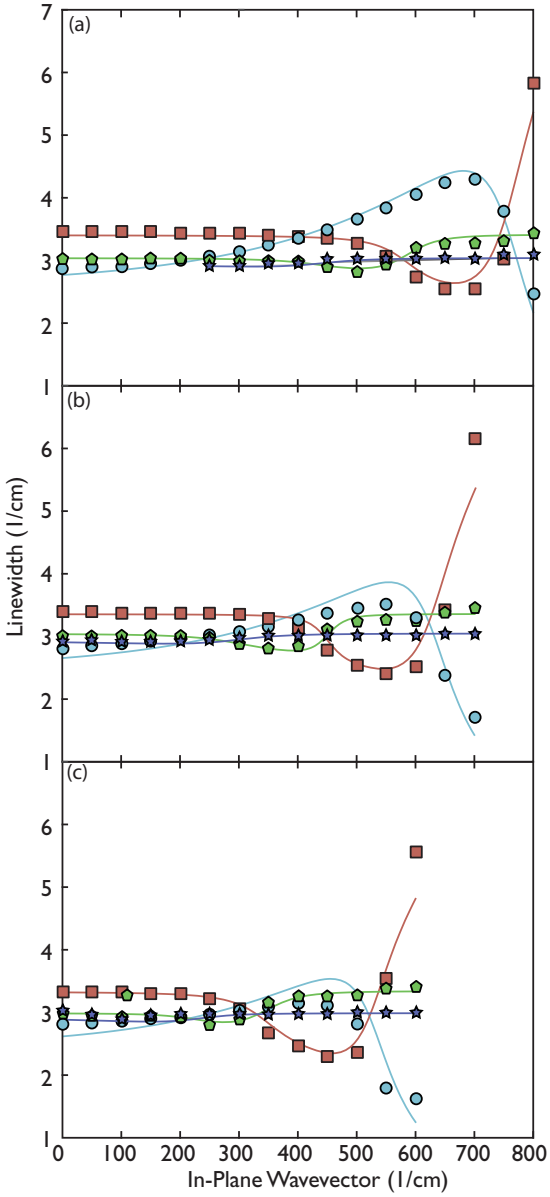


FIG. 6. Normal mode linewidths for array periods (a) 6 $\mu$m, (b) 6.5 $\mu$m, and (c) 7 $\mu$m. Symbols indicate numerical values. Lines indicate theoretical fits calculated utilizing Eq. (8). Each plot is truncated to restrict to the first Brillouin zone.

## V. CONCLUSION

We have investigated the morphology- and substrate-dependant phonon polariton resonances of cylindrical SiC nanoresonators by quasinormal modal analysis. Starting from the resonances of a single, free-standing cylinder, and then considering the impact of resonant coupling with surface phonon polariton modes sustained by the substrate, we were able to develop a complete and consistent understanding of those resonators. The present work will allow the easy design of novel samples with bespoke resonances, and it shines light on the nature of the hybrid localized-surface resonances, which will permit further investigations to explore different geometry and sample materials.

## ACKNOWLEDGMENTS

S.A.M. acknowledges support from EPSRC programme Grants No. EP/L024926/1 and No. EP/M013812/1, plus ONR Global, the Royal Society, and the Lee-Lucas Chair in Physics. S.D.L. has support from the Royal Society Research Fellowship program and he acknowledges support from EPSRC Grant No. EP/M003183/1.


## APPENDIX A: QUASINORMAL MODE THEORY

Under fairly general assumptions [17], the electromagnetic fields radiated by an emitter in the resonator $\Upsilon(\mathbf{r},\omega) = (\mathbf{E}(\mathbf{r},\omega),\mathbf{H}(\mathbf{r},\omega))$ can be linearly expanded onto a discrete set of quasinormal modes $\tilde{\Upsilon}_i(\mathbf{r}) = (\tilde{\mathbf{E}}_i(\mathbf{r}),\tilde{\mathbf{H}}_i(\mathbf{r}))$

$$\Upsilon(\mathbf{r},\omega) = \sum_i \alpha_i(\omega)\tilde{\Upsilon}_i(\mathbf{r}), \tag{A1}$$

where $\alpha_i(\omega)$ is a complex coefficient describing the relative contribution of the $i$th mode, and it has a pole at the complex modal frequency $\tilde{\omega}_i$. The quasinormal modes of the system are found using an iterative procedure to fit to a Pade approximated pole-like response function in the complex frequency plane, the iterative procedure is carried out utilizing the COMSOL Multiphysics FEM solver iteratively driven by a MATLAB code adapted from that distributed by Bai *et al.* [22].

On calculating the complex modal frequencies of the system we can immediately calculate the quality factor

$$Q_i = \frac{\mathrm{Re}[\tilde{\omega}_i]}{2\mathrm{Im}[\tilde{\omega}_i]}, \tag{A2}$$

as well as any other quantity of interest. In the neighborhood of the complex frequency $\tilde{\omega}_i$ it is an excellent approximation that the field scattered by the resonator is linearly proportional to the field of the quasinormal mode. It is therefore possible to calculate the mode volume through the equation

$$V_i = \frac{\int \left[\tilde{\mathbf{E}}_i \cdot \frac{\partial(\omega\epsilon(\mathbf{r},\omega))}{\partial\omega}\tilde{\mathbf{E}}_i - \tilde{\mathbf{H}}_i \cdot \frac{\partial(\omega\mu(\mathbf{r},\omega))}{\partial\omega}\tilde{\mathbf{H}}_i\right] d^3\mathbf{r}}{2\epsilon_0 n(\mathbf{r}_{\mathrm{dip}})^2[\tilde{\mathbf{E}}_i(\mathbf{r}_{\mathrm{dip}})\cdot\mathbf{u}]^2}, \tag{A3}$$

where the proportionality constants cancel from the numerator and denominator and the fields are evaluated very close to the complex resonant frequency. The emitter is located at $\mathbf{r}_{\mathrm{dip}}$. We truncate the simulation domain utilizing perfectly matched layers (PMLs) which convert outgoing radiative loss at the simulation boundary to dissipative loss in the PML domain providing a rigorous normalization [23].

The dispersive dielectric function of the matter is defined by the fitting parameters of Pitman [28] for 3C-SiC to the

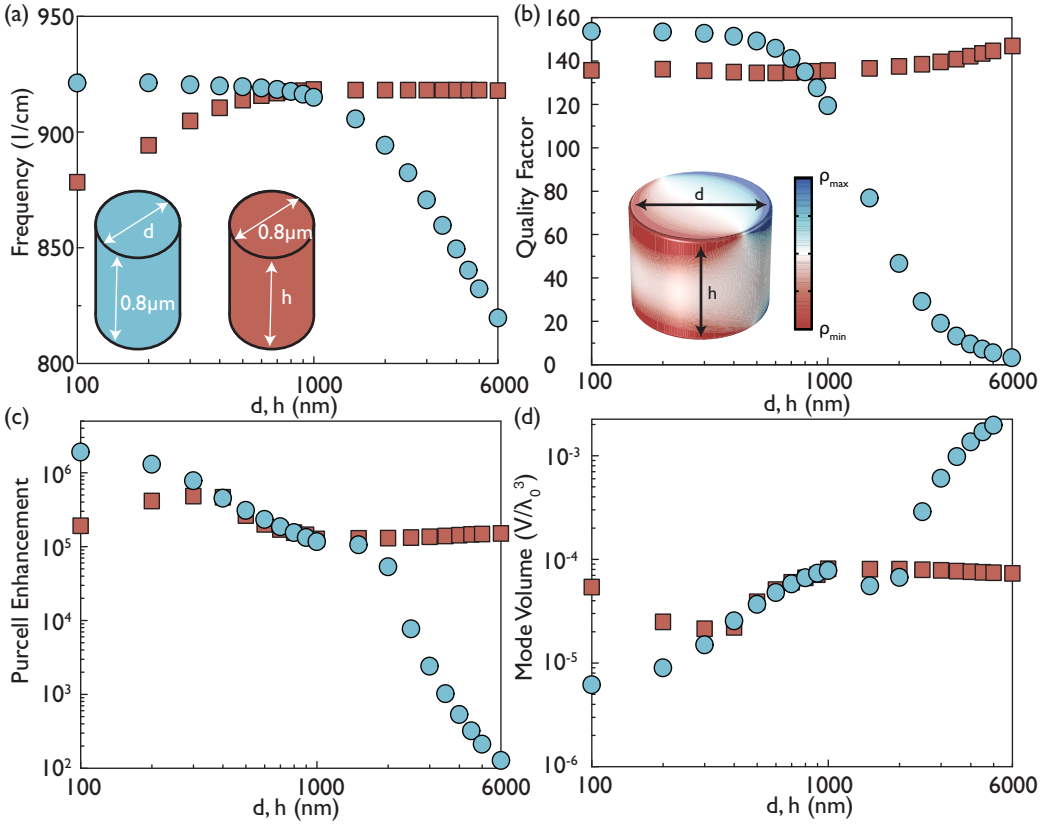


FIG. 7. (a) Real part of the resonant frequency of the dipolar transverse mode as a function of diameter at $h = 0.8$ $\mu$m (circles) and as a function of height at $d = 0.8$ $\mu$m (squares). (b) Quality factor of the dipolar transverse mode as a function of diameter at $h = 0.8$ $\mu$m (circles) and as a function of height at $d = 0.8$ $\mu$m (squares). Inset shows the surface charge distribution $\rho$ of the dipolar transverse mode for a cylinder of $h = 0.8$ $\mu$m and $d = 1$ $\mu$m. (c) Purcell enhancement of the dipolar transverse mode as a function of diameter at h=0.8 $\mu$m (circles) and as a function of height at d= 0.8 $\mu$m diameter (squares). (d) Mode volume of the dipolar transverse mode in units of the free space mode volume $\lambda_0^3$ as a function of diameter at $h = 0.8$ $\mu$m (circles) and as a function of height at $d = 0.8$ $\mu$m (squares).

functional form

$$\epsilon(\omega) = \epsilon_\infty + \frac{\omega_{\mathrm{LO}}^2(\epsilon_0 - \epsilon_\infty)}{\omega_{\mathrm{LO}}^2 - \frac{\epsilon_0}{\epsilon_\infty}\omega^2 - i\frac{\epsilon_0}{\epsilon_\infty}\gamma\omega}. \tag{A4}$$

This was used over an interpolated dielectric function to allow analytic continuation to the complex frequency plane. In passing from the standard definition of the mode volume to Eq. (A3), material dispersion is accounted for by taking the derivatives of the system dielectric function and the permeability. These derivatives are especially important in polar dielectric systems where the inflection of the dielectric function occurs entirely over the narrow bandwidth of the Reststrahlen band. The ratio of the dielectric function $\epsilon(\omega)$ in Eq. (A4) and the derivative $\omega\partial\epsilon(\omega)/\partial\omega$ exceeds unity throughout the Reststrahlen band, often lying between 10 and 100. This means that the contribution from the electric field energy in the polar dielectric increases by one to two orders of magnitude resulting in a substantial decrease in the achievable field confinements compared to the rudimentary Eq. (1), sometimes falling by up to two orders of magnitude. Physically this result arises from energy lying in the potential energy of the oscillating ions rather than in the electric field as illustrated in Fig. 1(b) [3].

Finally the Purcell enhancement for the $i$th mode may be calculated from the equation [18]

$$F_P = \frac{\Gamma}{\Gamma_0} = \frac{3}{4\pi^2}\left(\frac{\lambda_0}{n}\right)^3 \mathrm{Re}\left[\frac{Q_i}{V_i}\right], \tag{A5}$$

where $\Gamma(\Gamma_0)$ are the decay rates of a dipole in the presence of the resonator (in free space), $n$ is the refractive index at the dipole location, $\lambda_0$ is the free space wavelength, $Q_i$ and $V_i$ are as defined in the previous equations, and the real part of the ratio $Q_i/V_i$ is taken.

## APPENDIX B: TRANSVERSE DIPOLAR MODE

The resonant frequency of the dipolar transverse mode is investigated over the two-dimensional parameter space in Fig. 7(a). Squares correspond to a diameter scan at $h = 0.8$ $\mu$m and circles to a height scan at $d = 0.8$ $\mu$m. A red shift in the resonant frequency with increased diameter is observed, this occurs due to increased screening between charges at each cylinder edge. This increased screening pushes the mode frequency toward the transverse optical phonon frequency with an accompanying drop in quality factor, shown in Fig. 7(b) as observed for the monopolar mode in Fig. 1(b). In the large height limit $h \geqslant 1$ $\mu$m the resonant frequency reaches an asymptote as the dipoles at the end facets decouple; scanning the height weakly affects the quality factor as the mode is strongly localized at the cylinder end facets.

The surface charge distribution is illustrated on the inset in Fig. 7(a). The Purcell enhancement of the transverse mode is plotted in Fig. 7(c). Strong increases are observed in smaller geometries, exceeding $10^6$ as $d \to 0.1$ $\mu$m. These Purcell enhancements correspond to ultrasmall mode volumes less than $10^{-4}\lambda_0^3$ as shown in Fig. 7(d).

## APPENDIX C: PERIODIC RESONATOR ARRAYS

To achieve experimentally measurable observables it is necessary to measure arrays of resonators. In this paper we are restricted to square arrays of resonators. The modes of the coupled array is taken as a linear combination of the individual resonators quasinormal modes $\tilde{\mathbf{E}}_i(\mathbf{r})$ along a straight line parallel to the illumination wave vector which is taken parallel to an array principal axis. The dispersion of the mode of the periodic system may be approximated by the solution calculated in Ref. [29] for lossless systems in the tight binding approximation as

$$\omega_{\mathbf{k}_\parallel}^i = \omega^i\left(1 - \frac{\Delta\gamma}{2} + (\beta_1 - \gamma_1)\cos\left(k_\parallel R\right)\right), \tag{C1}$$

where $\omega_{\mathbf{k}_\parallel}^i$ is the dispersive frequency, $\mathbf{k}_\parallel$ is the in-plane wave vector, $\omega^i$ is the frequency of the isolated resonator mode, and $\Delta\gamma$, $\beta_1$, $\gamma_1$ are as defined in Ref. [29].

The strength of inter-resonator coupling is investigated for square arrays of cylinders in vacuum and on a substrate. The cylinders are of height 0.8 $\mu$m and diameter 1 $\mu$m. The inter-resonator gap is varied to assess the coupling at the $\mathbf{k}_\parallel = 0$ point. Symbols in Fig. 8 represent the real frequencies calculated from the pole fitting algorithm, lines represent fits to the results assuming a simple $1/r^3$ dipole-dipole coupling. In each case the longitudinal mode and lowest lying transverse mode are studied. The longitudinal mode blue shifts as the inter-resonator gap is decreased; this is because the dipoles are orientated in the same direction along the cylinder long axis, repulsing each other. Conversely the transverse mode red shifts as the inter-resonator gap is decreased, because

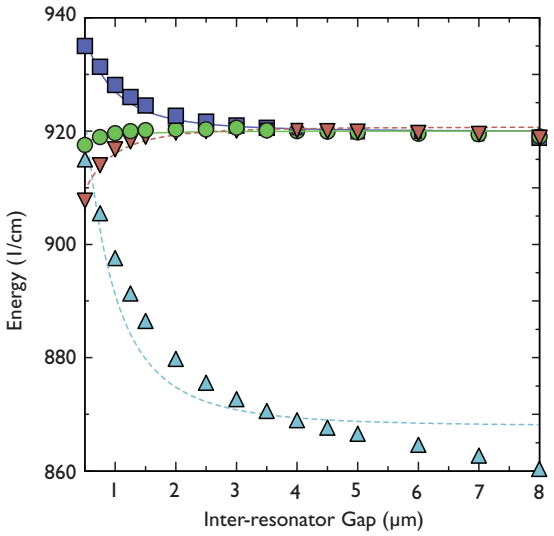


FIG. 8. Symbols represent the real resonant frequencies calculated from the pole fitting algorithm at the $\mathbf{k}_\parallel = 0$ point for a square array of cylinders of height 0.8 $\mu$m and diameter 1 $\mu$m. Purple squares (green circles) represent the longitudinal (lowest transverse) mode in free cylinders. Blue triangles (red inverted triangles) represent the longitudinal (lowest transverse) mode for cylinders in contact with an SiC substrate. The overlapping lines represent a fit with a simple dipole-dipole coupling model.

dipoles facing each other on neighboring cylinders are aligned in opposite directions and they attract each other. Larger shifts are observed for the resonators on substrate, this is because the substrate is highly reflective in the Reststrahlen band and more radiative emission from each resonator propagates to the next. From Fig. 8 it is also clear that the monopolar mode is much more dispersive than the transverse one. This is a general feature because the monopolar mode generates a flow of charge between the pillars and the interpillar surfaces [8], increasing the coupling. For this reason, in the fitting procedure outlined in the text, we only considered the dispersion of the monopolar mode, leading to the two fitting parameters $\alpha = \omega^m(1 - \Delta\gamma/2)$ and $\zeta = \omega^m(\beta_1 - \gamma_1)$, with $\omega^m$ the frequency of the monopolar mode in the single cylinder.


[1] S. A. Maier, *Plasmonics: Fundamentals and Applications* (Springer, New York, 2007).

[2] R. Hillenbrand, T. Taubner, and F. Keilmann, Phonon-enhanced light-matter interaction at the nanometre scale, Nature **418**, 159 (2002).

[3] J. B. Khurgin, How to deal with the loss in plasmonics and metamaterials, Nat. Nanotech. **10**, 2 (2015).

[4] G. Borstel, H. J. Falge, and A. Otto, Surface and bulk phonon-polaritons observed by attenuated total reflection, Springer Tracts Mod. Phys. **74**, 107 (1974).

[5] H. Mutschke, A. C. Andersen, D. Clement, T. Henning, and G. Peiter, Infrared properties of SiC particles, Astron. Astrophys. **345**, 187 (1999).

[6] J.-J. Greffet *et al.*, Coherent emission of light by thermal sources, Nature **416**, 61 (2002).

[7] J. A. Schuller, T. Taubner, and M. L. Brongersma, Optical antenna thermal emitters, Nat. Photon. **3**, 658 (2009).

[8] J. D. Caldwell *et al.*, Low-loss, extreme subdiffraction photon confinement via silicon carbide localized surface phonon polariton resonators, Nano Lett. **13**, 3690 (2013).

[9] Y. Chen *et al.*, Spectral tuning of localized surface phonon polariton resonators for low-loss mid-IR applications, ACS Photonics **1**, 718 (2014).

[10] C. R. Gubbin, F. Martini, A. Politi, S. A. Maier, and S. De Liberato, Strong and Coherent Coupling between Localized and Propagating Phonon Polaritons, Phys. Rev. Lett. **116**, 246402 (2016).

[11] T. Taubner, D. Korobkin, Y. Urzhumov, G. Shvets, and R. Hillenbrand, Near-field microscopy through a SiC superlens, Science **313**, 1595 (2006).

[12] T. Taubner, F. Keilmann, and R. Hillenbrand, Nanomechanical resonance tuning and phase effects in optical near-field interaction, Nano Lett. **4**, 1669 (2004).

[13] S. Shen, A. Narayanaswamy, and G. Chen, Surface phonon polaritons mediated energy transfer between nanoscale gaps, Nano Lett. **9**, 2909 (2009).

[14] C. F. Bohren and D. R. Huffman, *Absorption and scattering of light by small particles* (Wiley, New York, 1983).

[15] H. Ditlbacher, A. Hohenau, D. Wagner, U. Kreibig, M. Rogers, F. Hofer, F. R. Aussenegg, and J. R. Krenn, Silver Nanowires as Surface Plasmon Resonators, Phys. Rev. Lett. **95**, 257403 (2005).

[16] R. K. Chang and A. J. Campillo, *Optical Processes in Microcavities* (World Scientific, Singapore, 1996).

[17] P. T. Leung, S. Y. Liu, and K. Young, Completeness and orthogonality of quasinormal modes in leaky optical cavities, Phys. Rev. A **49**, 3057 (1994).

[18] C. Sauvan, J. P. Hugonin, I. S. Maksymov, and P. Lalanne, Theory of the Spontaneous Optical Emission of Nanosize Photonic and Plasmon Resonators, Phys. Rev. Lett. **110**, 237401 (2013).

[19] P. T. Kristensen and S. Hughes, Modes and mode volumes of leaky optical cavities and plasmonic nanoresonators, ACS Photonics **1**, 2 (2013).

[20] A. F. Koenderink, On the use of Purcell factors for plasmonic antennas, Opt. Lett. **35**, 4208 (2010).

[21] R. Ruppin, Electromagnetic energy density in a dispersive and absorptive material, Phys. Lett. A **299**, 309 (2002).

[22] Q. Bai, M. Perrin, C. Sauvan, J. P. Hugonin, and P. Lalanne, Efficient and intuitive method for the analysis of light scattering by a resonant nanostructure, Opt. Express **21**, 27371 (2013).

[23] E. A. Muljarov and W. Langbein, Exact mode volume and purcell factor of open optical systems, Phys. Rev. B **94**, 235438 (2016).

[24] J. Takahara, Guiding of a one-dimensional optical beam with nanometer diameter, Opt. Lett. **22**, 475 (1997).

[25] P. Nordlander and E. Prodan, Plasmon hybridization in nanoparticles near metallic surfaces, Nano Lett. **4**, 2209 (2004).

[26] C. Gubbin, S. A. Maier, and S. De Liberato, Real-space Hopfield diagonalization of inhomogeneous dispersive media, Phys. Rev. B **94**, 205301 (2016).

[27] J. J. Hopfield, Theory of the contribution of excitons to the complex dielectric constant of crystals, Phys. Rev. **112**, 1555 (1958).

[28] K. M. Pitman, A. M. Hofmeister, A. B. Corman, and A. K. Speck, Optical properties of silicon carbide for astrophysical applications I. New laboratory infrared reflectance spectra and optical constants, Astron. Astrophys. **483**, 661 (2008).

[29] A. Yariv *et al.*, Coupled-resonator optical waveguide: A proposal and analysis, Opt. Lett. **24**, 711 (1999).